

Modeling the electromagnetic properties of the SCUBA-2 detectors

Michael D. Audley^a, Giampaolo Pisano^b, Wayne S. Holland^a, William D. Duncan^c, William Parkes^d, and Peter A. R. Ade^b

^aUK Astronomy Technology Centre, Royal Observatory, Edinburgh, EH9 3HJ, UK;

^bCardiff University, Cardiff, CF24 3YB, UK;

^cNational Institute of Standards and Technology, 325 Broadway, Boulder, CO 80305, USA;

^dThe Scottish Microelectronics Centre, University of Edinburgh, Edinburgh, EH9 3JF, UK

Copyright 2004 Society of Photo-Optical Instrumentation Engineers.

This paper will be published in SPIE conference proceedings volume 5498, “Millimeter and Submillimeter Detectors for Astronomy II.” and is made available as an electronic preprint with permission of SPIE. One print or electronic copy may be made for personal use only. Systematic or multiple reproduction, distribution to multiple locations via electronic or other means, duplication of any material in this paper for a fee or for commercial purposes, or modification of the content of the paper are prohibited.

ABSTRACT

SCUBA-2 is the next-generation replacement for SCUBA (Sub-millimetre Common User Bolometer Array) on the James Clerk Maxwell Telescope. Operating at 450 and 850 μm , SCUBA-2 fills the focal plane of the telescope with fully-sampled, monolithic bolometer arrays. Each SCUBA-2 pixel uses a quarter-wave slab of silicon with an implanted resistive layer and backshort as an absorber and a superconducting transition edge sensor as a thermometer. In order to verify and optimize the pixel design, we have investigated the electromagnetic behaviour of the detectors, using both a simple transmission-line model and Ansoft HFSS™, a finite-element electromagnetic simulator. We used the transmission line model to fit transmission measurements of doped wafers and determined the correct implant dose for the absorbing layer. The more detailed HFSS modelling yielded some unexpected results which led us to modify the pixel design. We also verified that the detectors suffered little loss of sensitivity for off-axis angles up to about 30°.

Keywords: SCUBA-2, Sub-millimetre bolometer array, Electromagnetic modeling

1. INTRODUCTION

In SCUBA-2¹ two detector arrays will observe simultaneously at wavelengths (λ) of 850 and 450 μm . Each array consists of four 40×32 sub-arrays of square pixels. Each pixel comprises a silicon slab which has a metal layer, or *backshort*, behind it. For the interface between free space and the front of the slab, the reflection coefficient is

$$R = \left(\frac{1 - n}{1 + n} \right)^2 \quad (1)$$

where n is the refractive index of the slab. We assume $n = 3.388$ for cold silicon, giving $R = 30\%$. However, we can reduce the reflectivity (and thus maximize the detector efficiency) if the thickness of the slab is chosen so that the radiation reflected by the backshort at the back of the slab interferes destructively with the radiation reflected by the top of the slab. In both cases, the radiation undergoes a 180° phase change on reflection, so the slab thickness is chosen to be an odd multiple of $\lambda/4$ in the slab material. This arrangement is known as a Salisbury screen and is used in aviation for reducing radar reflections. The operation of the detector is shown in Figure 1. At sub-millimetre wavelengths and low temperatures, silicon has negligible dissipation. Thus, the slab has an implanted resistive layer at the top to dissipate the energy of the radiation, heating up the pixel.

Further author information: (Send correspondence to M.D.A.)

M.D.A.: E-mail: mda@roe.ac.uk, Website: <http://www.roe.ac.uk/atc/projects/scubatwo/>

To maximize the detector efficiency, we need to choose the implantation dose so that the surface resistance is $R_s \approx 377 \Omega/\square$, matching the wave impedance of free space ($Z_0 = 120 \pi \Omega$). The temperature rise due to the absorption of radiation is detected by a transition-edge sensor (TES) on the back side of the quarter-wave slab. It is this TES that acts as the reflective backshort.

The pixel geometry is repeated across the detector wafer to form one of SCUBA-2's 40×32 sub-arrays. Each sub-array is bump-bonded to a wafer that carries the SQUID multiplexing (MUX) circuitry. The indium bump bonds provide electrical and thermal connections, as well as mechanical strength.

The size of an individual quarter-wave slab ($1055 \mu\text{m}$, allowing for the wall thickness and the gap between the walls and slab) is on the order of the wavelength of the incident radiation (850 and $450 \mu\text{m}$). This means that to design the pixels for maximum efficiency we need a model of the electromagnetic behavior of the detector. We need answers to the following questions. How should we design the pixels to maximize the detector efficiency, and how much variation in the detector parameters can we tolerate? How does the efficiency of the detector depend on the wavelength, polarization, and incident angle? To answer these questions, we carried out electromagnetic modeling. We approached the problem in two ways. First, we modeled the detectors as a simple transmission line. This model is equivalent to an infinite dielectric slab absorber and does not take into account any effects due to the finite size of the pixels, the supporting grid, or the periodicity of the array. Then, we used a commercial software package, Ansoft HFSSTM (High-Frequency Structure Simulator; see <http://www.ansoft.com>), to model the behaviour of the detectors more realistically. HFSS is a three-dimensional finite-element method electromagnetic simulator.

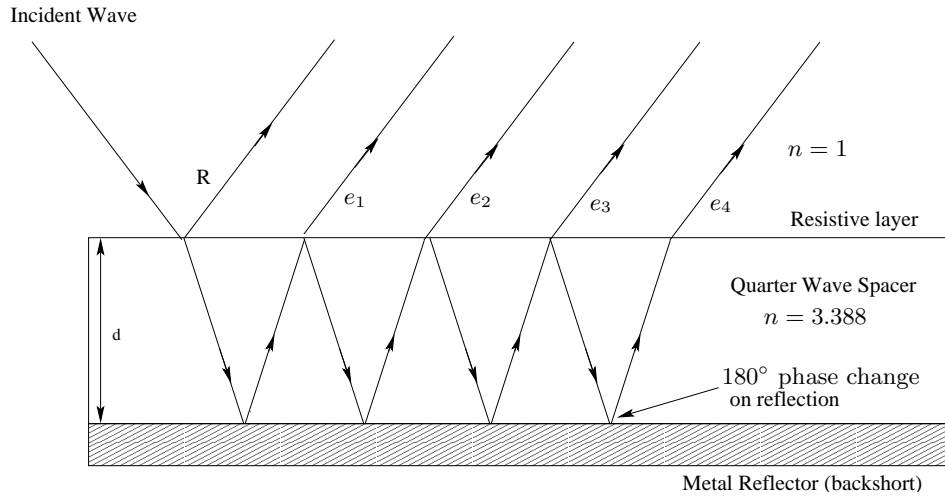


Figure 1. Operation of the SCUBA-2 pixels. The detectors consist of a metal reflector and a resistive layer spaced a quarter wavelength apart by a slab of silicon. This arrangement is known as a Salisbury screen. The emergent waves (e_i) interfere destructively with the reflected wave (R) and constructively with the incident wave. This maximizes the energy dissipated in the resistive layer at the top of the quarter-wave slab and minimizes the amount reflected.

2. TRANSMISSION LINE MODEL

For a simple model we can represent the vacuum, silicon, metal sandwich as a transmission line with corresponding impedances (see Figure 2). Because we are assuming that the pixels extend laterally to infinity, we neglect any effects due to the finite size of the pixels or the periodicity of the array. These effects will be addressed in Section 3. Using this simple transmission line model, the voltage transmission coefficient is

$$t = \frac{4 e^{i 4 \pi n d \sigma} n z_s z_t}{(1 - (n - 1) z_s) ((n - 1) z_t - 1) + e^{i 4 \pi n d \sigma} (1 + z_s + n z_s) (1 + z_t + n z_t)} \quad (2)$$

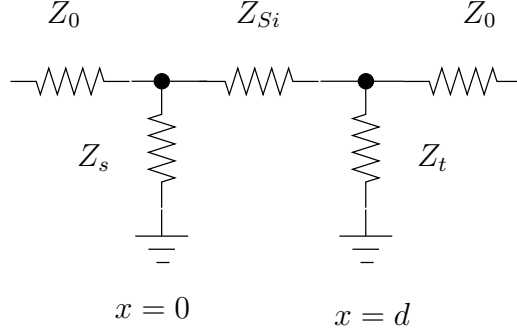


Figure 2. SCUBA-2 quarter-wave slab represented by a simple transmission line model. The slab has a thickness d . The surface impedances of its front and rear faces are Z_s and Z_t . The dielectric of refractive index n is represented by an impedance $Z_{Si} = Z_0/n$, where Z_0 is the impedance of free space. For the SCUBA-2 pixels we have $R_s = 377 \, \Omega/\square$ and $Z_t \rightarrow 0$.

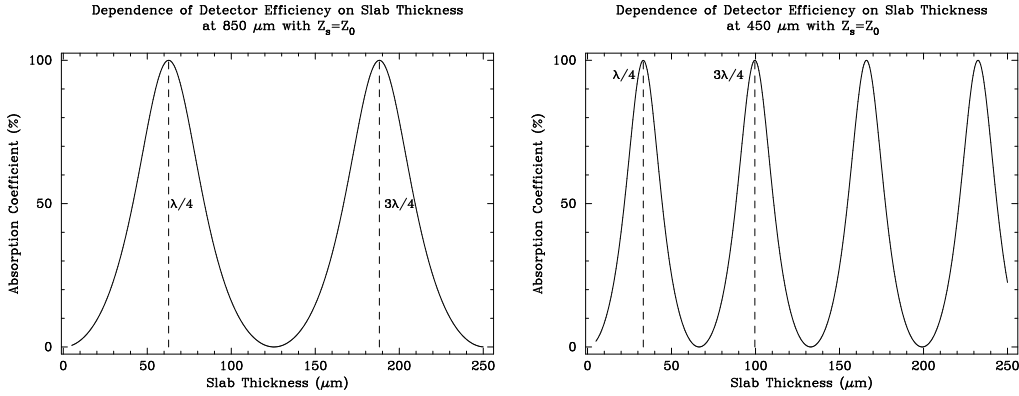


Figure 3. Dependence of quarter-wave slab absorption coefficient on slab thickness predicted from the simple transmission line model for wavelengths of 850 (left) and 450 μm (right). The quarter-wave slab has a resistive layer on the front with $R_s = Z_0$.

and the voltage reflection coefficient is

$$r = \frac{(z_s + n z_s - 1) ((n-1) z_t - 1) - e^{i 4\pi n d \sigma} ((n-1) z_s + 1) (1 + z_t + n z_t)}{(1 - (n-1) z_s) ((n-1) z_t - 1) + e^{i 4\pi n d \sigma} (1 + z_s + n z_s) (1 + z_t + n z_t)} \quad (3)$$

where $z_s = Z_s/Z_0$ and $z_t = Z_t/Z_0$. The corresponding power transmission, reflection, and absorption coefficients are $T = |t|^2$, $R = |r|^2$, and $A = 1 - T - R$, respectively. In the general case, these expressions are complicated.

To model the behaviour of the SCUBA-2 detectors, we let $z_t \rightarrow 0$ in Equation 2. This means that we are assuming that the back of the slab is covered by a perfect conductor (the backshort). Figures 3 and 4 show how the predicted absorption coefficients depend on the slab thickness and the wavelength of the incident radiation. We are assuming that the implanted absorbing layer is purely resistive. Note that the $\frac{3}{4}\lambda$ slab of the 450 μm detectors has greater wavelength selectivity than the $\frac{1}{4}\lambda$ slab of the 850 μm detectors.

2.1. Angular Dependence

In the current design, the SCUBA-2 optics are not telecentric. Pixels at the edges of the arrays will have rays incident on them at angles up to about 18° . Thus, we must ensure that the efficiency of the detectors does not fall off too rapidly with incident angle. Otherwise, pixels near the edges of the arrays will be insensitive. We used the simple transmission line model to investigate the angular dependence of the detector efficiency. We generalized the model to oblique incidence by making the substitutions shown in Table 1.^{2,3} For normal incidence, the

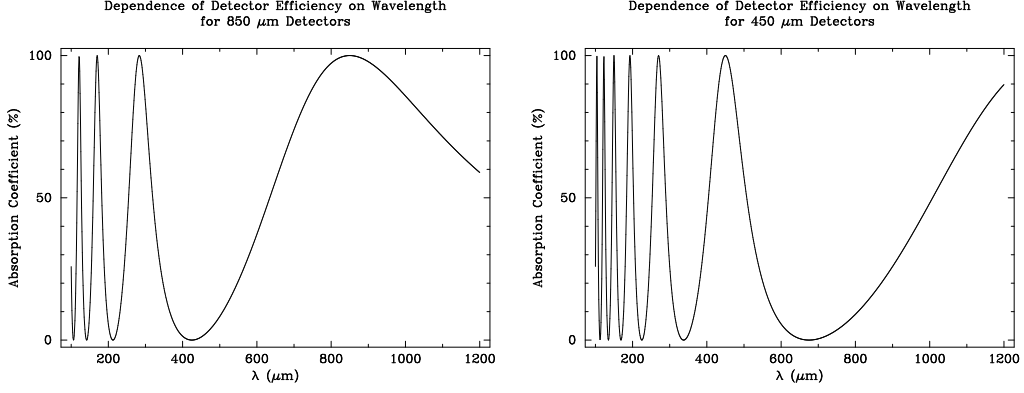


Figure 4. Wavelength dependence of absorption coefficient of quarter-wave slab predicted from the simple transmission line model. Left: Slab thickness $d = 62.7 \mu\text{m}$ ($850 \mu\text{m}$ detector). Right: Slab thickness $d = 99.6 \mu\text{m}$ ($450 \mu\text{m}$ detector). The quarter-wave slab has a resistive layer on the front with $R_s = Z_0$.

Table 1. Substitutions to generalize transmission line model to case of oblique incidence. $\Re(Z_{Si})$ is the real part of Z_{Si} .

Quantity	Normal incidence	Oblique Incidence	
		s-polarization	p-polarization
Free-space impedance	Z_0	$Z_0 \cos \theta$	$Z_0 / \cos \theta$
Slab impedance	Z_{Si}	$Z_{Si} \cos(\arcsin(\frac{\Re(Z_{Si}) \sin \theta}{Z_0}))$	$Z_{Si} / \cos(\arcsin(\frac{\Re(Z_{Si}) \sin \theta}{Z_0}))$
Slab thickness	d	$d \cos(\arcsin(\frac{\Re(Z_{Si}) \sin \theta \cos \theta}{Z_0}))$	$d \cos(\arcsin(\frac{\Re(Z_{Si}) \sin \theta \cos \theta}{Z_0}))$

two linear polarizations are equivalent. However, for oblique incidence, we must treat the s-polarization (E-field parallel to the plane of incidence) and the p-polarization (E-field normal to the plane of incidence) separately.

Using the substitutions in Table 1 with the transmission line model we calculated the angular dependence of the efficiencies of the SCUBA-2 detectors for s- and p-polarized radiation. The results are shown in Figure 5. We found that the $\frac{3}{4}\lambda$ slab of the $450 \mu\text{m}$ detectors has greater polarization-dependence than the $\frac{1}{4}\lambda$ slab of the $850 \mu\text{m}$ detectors.

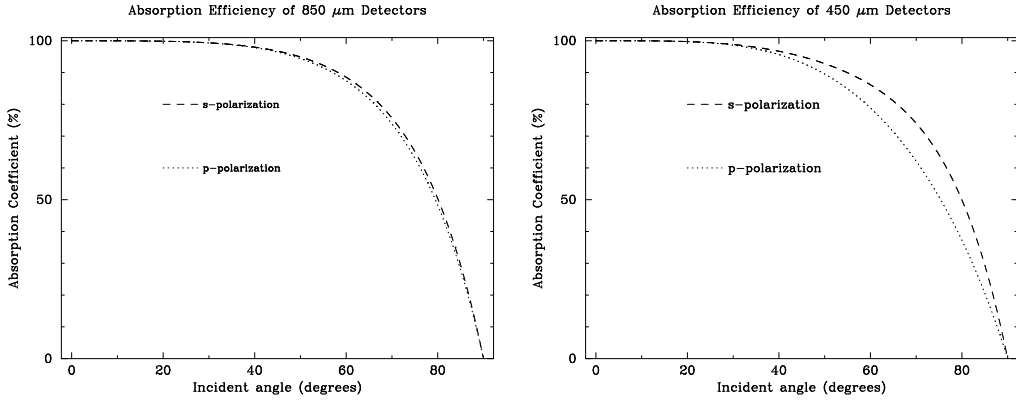


Figure 5. Angular dependence of absorption efficiency of SCUBA-2 $850 \mu\text{m}$ (left) and $450 \mu\text{m}$ (right) detectors for s- and p-polarized radiation, predicted from the simple transmission line model.

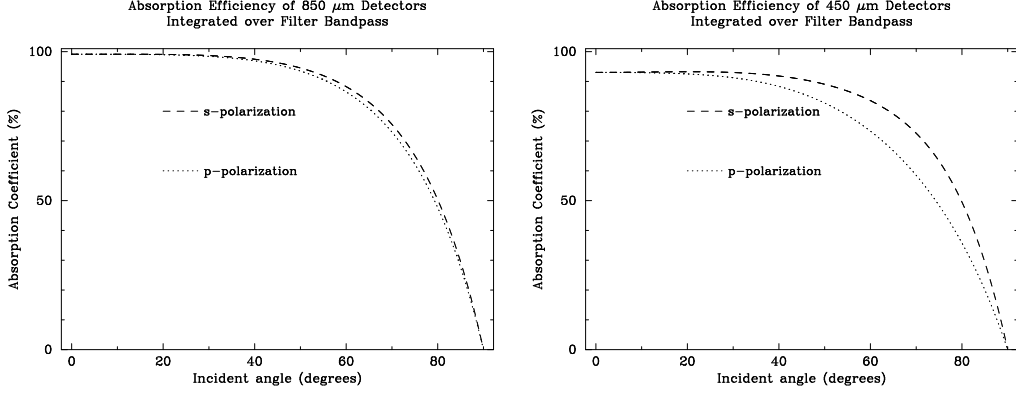


Figure 6. Angular dependence of absorption efficiency of SCUBA-2 850 μm (left) and 450 μm (right) detectors for s- and p-polarized radiation, predicted from the simple transmission line model assuming a 10% frequency bandpass (modeled as a double Gaussian). The on-axis efficiency is degraded to 99.14% of its monochromatic value for the 850 μm detectors and 93.35% for the 450 μm detectors.

2.2. Effect of Filter Bandpass

The radiation incident on the SCUBA-2 detectors will not be monochromatic. To investigate the effect of the finite bandpass of the SCUBA-2 filters, we smeared the results of the transmission line model over a double-Gaussian filter function with a frequency bandpass of 10%. The effect of smearing over the filter bandpass is slight in the case of the 850 μm detectors. However, for the 450 μm detectors the on-axis efficiency is degraded to 93.35% of its monochromatic value. The results are shown in Figure 6. The difference between the 850 and 450 μm detectors is not unexpected. As was shown in Figure 4, the 450 μm detectors have greater wavelength selectivity.

2.3. Implant Dose

Our first application of the transmission line model to real data was to determine the correct implant dose for the implanted layer that absorbs the incident radiation. Wafers were implanted on the front side with different doses. The implantation process is described elsewhere in these proceedings.⁴ The submillimetre transmission of the wafers was measured at 1.5 K as a function of wavenumber (σ) using a Fourier transform spectrometer at Cardiff University. To model the transmission of these implanted wafers, we let $z_t \rightarrow \infty$ in Equation 2. We found that the model gave a satisfactory fit only if we added another component to the model — an overall normalization factor — and allowed this to vary freely. The fits are consistent with the implanted layer being purely resistive rather than metallic. Assuming we have a purely resistive implanted layer, as long as the correct thickness is chosen for the quarter-wave spacer the absorption efficiency does not depend strongly on the surface resistance R_s (see Figure 7).

3. FINITE-ELEMENT MODELING WITH ANSOFT HFSS

3.1. Description of the Software

The simulations described here were carried out using HFSS version 8.5. HFSS includes a three-dimensional drawing program that can be used to construct a geometrical model. In other parts of the software, the user specifies the material properties, boundary conditions, and electromagnetic excitation of the model. HFSS divides the volume of the model into a mesh of tetrahedra and solves for the electric field on the mesh in the frequency domain. The problem is converted into a set of linear equations, represented by a matrix. A field solution is obtained by inverting the matrix for the initial mesh. The mesh is then refined, based on the local field strength. The field solution from the refined mesh is compared with the previous solution. This process of refinement and solving continues until the user-specified convergence criteria are met. The convergence criteria depend on the type of excitation. For the models described here the model is excited with an incident planewave and convergence is evaluated from changes in the total scattered energy, calculated from the E-field.

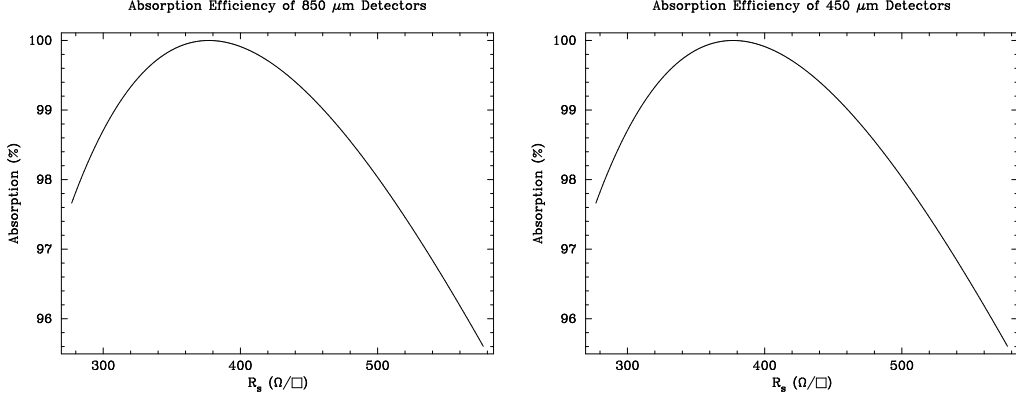


Figure 7. Dependence of absorption efficiency of SCUBA-2 850 (left) and 450 μm (right) detectors on surface resistance R_s predicted from the simple transmission line model.

HFSS includes tools for visualizing the field solutions and calculating physical quantities from them. These may be run from scripts to calculate quantities such as the reflection and absorption coefficients automatically. We used the Ansoft Optimetrics™ package to run HFSS repeatedly on models while varying geometric or material parameters.

3.2. Description of the Models

3.2.1. Method

We simulated an infinite array of pixels by modeling a single square pixel and applying periodic boundary conditions to opposite walls. The models are excited by an incident plane wave. HFSS solves for the E-field in the model. From the E-field we can calculate the physical quantities that interest us. These are the power absorbed in the resistive layer, the total incident and reflected power, and the power flowing in or out of the unit cell through the side walls. The power absorbed in the implanted resistive layer is calculated from the field on the surface:

$$P_{abs} = \frac{1}{2R_s} \int_S (\mathbf{E} \times \hat{\mathbf{n}})^2 dS \quad (4)$$

where R_s is the surface resistance of the implanted layer and $\hat{\mathbf{n}}$ is the unit normal to the surface. We have assumed $R_s = 377 \Omega/\square$ for all of the models. The other powers are found by integrating the Poynting vector over the appropriate surfaces.

Our basic pixel model consists of an approximation to a unit cell of the array (see Figure 8). Vertical boundaries run through the centres of the silicon walls. The walls are $50 \mu\text{m}$ thick, so that the unit cell contains the half-width of $25 \mu\text{m}$. Periodic boundary conditions are applied to opposite side walls. In the original pixel design there was a supporting grid $381 \mu\text{m}$ high on top of the walls. This was later removed from the design (see Section 4.3). The results presented here are for models without this grid, unless otherwise stated. The volume of the model extends $1\frac{1}{4}$ wavelengths above the top of the walls (or grid, if present). Inside the walls is the quarter-wave silicon slab with a resistive layer on its top surface. Under the slab is a perfectly conducting layer, to simulate the superconducting TES.

3.2.2. Selection of boundary conditions

For the top of the model where the waves come in, we have a choice of radiation boundary or perfectly matched layer (PML). Both of these are designed to emulate free space by absorbing incident radiation. The radiation boundary will absorb normally-incident radiation but it has a finite reflectivity for large angles of incidence. The PML is a lossy, anisotropic dielectric that will also absorb radiation incident at large angles. Because we wanted to illuminate the pixels with radiation incident at oblique angles, we chose a PML for the top of the model.

On the side walls, we apply periodic boundary conditions for consistency with the plane wave excitation. The periodic boundary conditions on the pixel walls result in an asymmetric matrix, which increases the problem

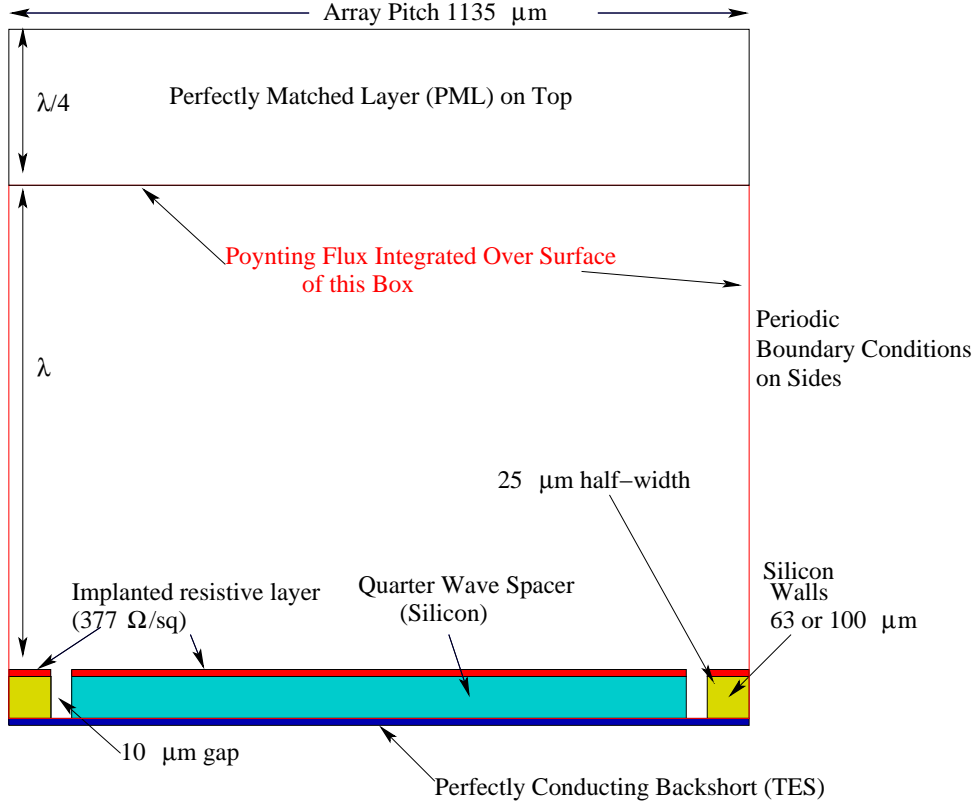


Figure 8. Pixel model used in HFSS simulations.

size. However, neither radiation boundaries or PMLs are suitable for the side walls and yield results inconsistent with energy conservation.

3.2.3. Error Analysis

Because HFSS provides no direct measure of the errors in the results, we needed to find some way to check the quality of solutions. The results can be checked for consistency by accounting for all of the incident power flowing into the unit cell. The integrated flux flowing through all the walls of the model plus the power absorbed in the resistive layer of the quarter-wave slab should add up to the incident power. Any difference should be small for a high-quality solution. In the plots below, the error bars on the absorption and reflection coefficients are derived from this discrepancy in the total power. While they are not useful for deriving statistical uncertainties, they are shown so that the relative accuracy of the solutions can be compared. Another way to evaluate the solution is to calculate the incident power flowing through the upper boundary and compare it with the Poynting flux integrated over the surface. The results should be slightly different due to the finite size of the mesh elements. In HFSS, for plane wave excitation, the default setting is to apply a free-space plane wave with a peak electric field of 1 V m^{-1} . From this we can calculate the incident flux as

$$P_{inc} = \int_A \mathbf{S} \cdot d\mathbf{A} = \frac{1}{2} \mathbf{E} \times \mathbf{H} A \cos \theta = \frac{1}{2} \sqrt{\frac{\epsilon_0}{\mu_0}} E^2 A \cos \theta \quad (5)$$

where A is the area of the top surface of the model, and θ is the angle of incidence. The factor of $1/2$ arises from the fact that the HFSS field calculator uses peak phasors to represent the fields. We found that the incident flux calculated from Equation 5 sometimes differed from the integrated Poynting flux by up to 10%. Thus, in the results given below, the incident flux is derived from Equation 5.

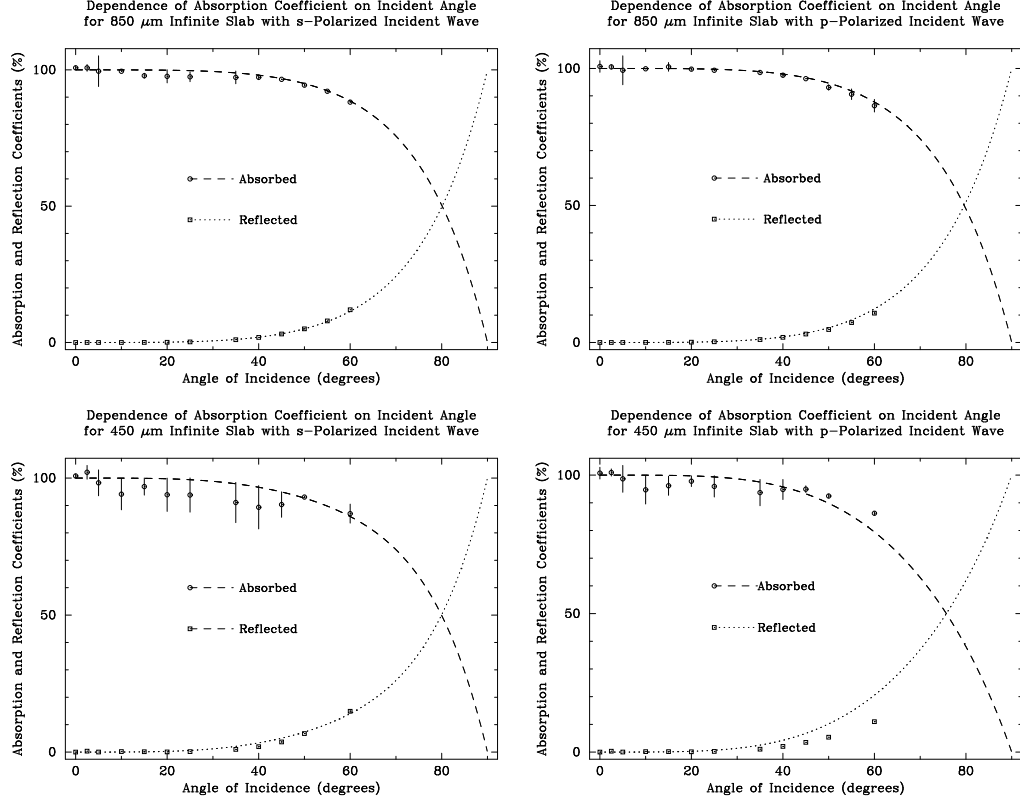


Figure 9. Comparison of results from HFSS (points) and the simple transmission line model (lines) for a Salisbury screen.

In order to check the accuracy of the HFSS solutions we simulated the 850 and 450 μm detectors as infinite slabs and compared the results with those from the transmission line model. Figure 9 shows good agreement for both, although the 450 μm efficiency is underestimated and has greater uncertainty. This is because the shorter wavelength requires a finer mesh for the same precision. The ultimate limit on the precision of the field solution is memory. This limits the total number of tetrahedra in the mesh. The version of HFSS we used is a 32-bit program. This means that it will fail if the mesh grows to more than 4 GB. In order to obtain the best precision possible, we pushed the mesh refinement until this limit was reached when solving our models.

4. RESULTS OF THE HFSS MODELING

4.1. Detection Efficiency

We used the Ansoft Optimetrics package to investigate how the absorption coefficient varied with the thickness of the quarter-wave slab. The results are shown in Figure 10. For the 850 μm detectors the absorption coefficient is greatest with a slab thickness of $\sim 65 \mu\text{m}$. From the assumed value of the refractive index ($n = 3.388$) we would expect the maximum to occur at a slab thickness of $62.7 \mu\text{m}$ which corresponds to $\lambda/4$ in silicon. For the 450 μm detectors the maximum occurs close to the expected value of $100 \mu\text{m}$ ($3\lambda/4$). In each case the peak monochromatic detection efficiency was 94%.

4.2. Angular dependence

We investigated the off-axis response of both the 850 and 450 μm detectors with the Ansoft Optimetrics package. Neither detector suffers much loss in sensitivity for incident angles up to 30° (see Figure 11). However, this sensitivity to oblique radiation does make the detectors susceptible to stray light.

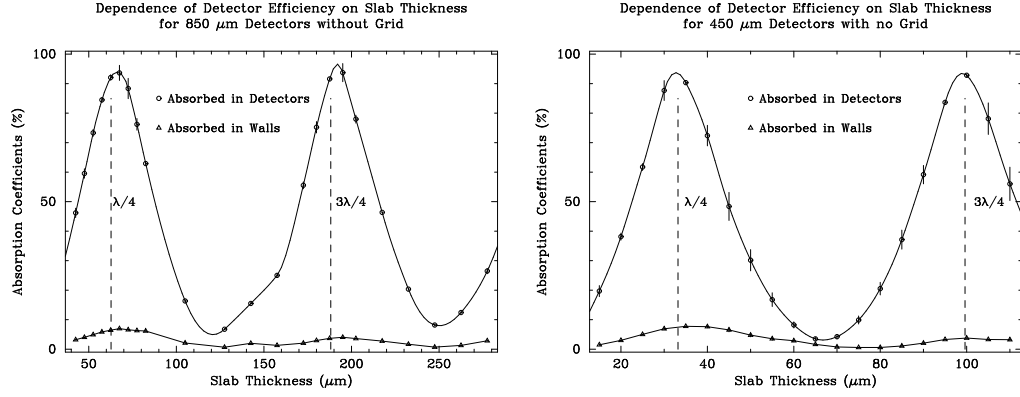


Figure 10. Predicted variation of detector efficiency with quarter-wave slab thickness for 850 μm (left) and 450 μm (right) detectors from HFSS simulations. The vertical dashed lines correspond to the expected thicknesses for maximum efficiency.

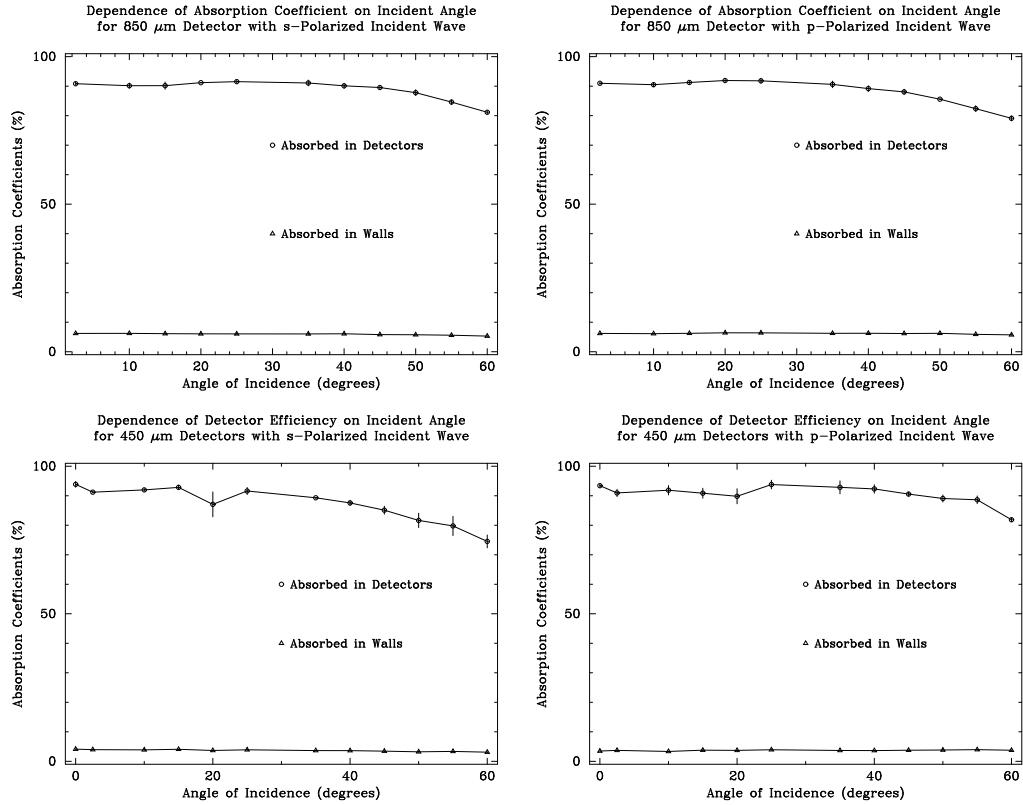


Figure 11. Predicted variation of 850 μm (top) and 450 μm (bottom) detector efficiency with angle of incidence from HFSS simulations. Left: s-polarization. Right: p-polarization.

4.3. Effect of Supporting Grid

The original design for the SCUBA-2 pixels had a silicon grid supporting the detector wafers. A model that includes this grid is shown in Figure 12. This grid was essentially an extension of the side walls by $381\text{ }\mu\text{m}$, a standard wafer thickness. The purpose of the grid was to provide mechanical rigidity to the detector array. Since silicon is essentially transparent at these wavelengths, its effect on the detector performance was thought to be insignificant. However, the HFSS modeling revealed that the grid acted as a dielectric waveguide, both reducing the detector efficiency and changing the optimum slab thickness (see Figure 13).

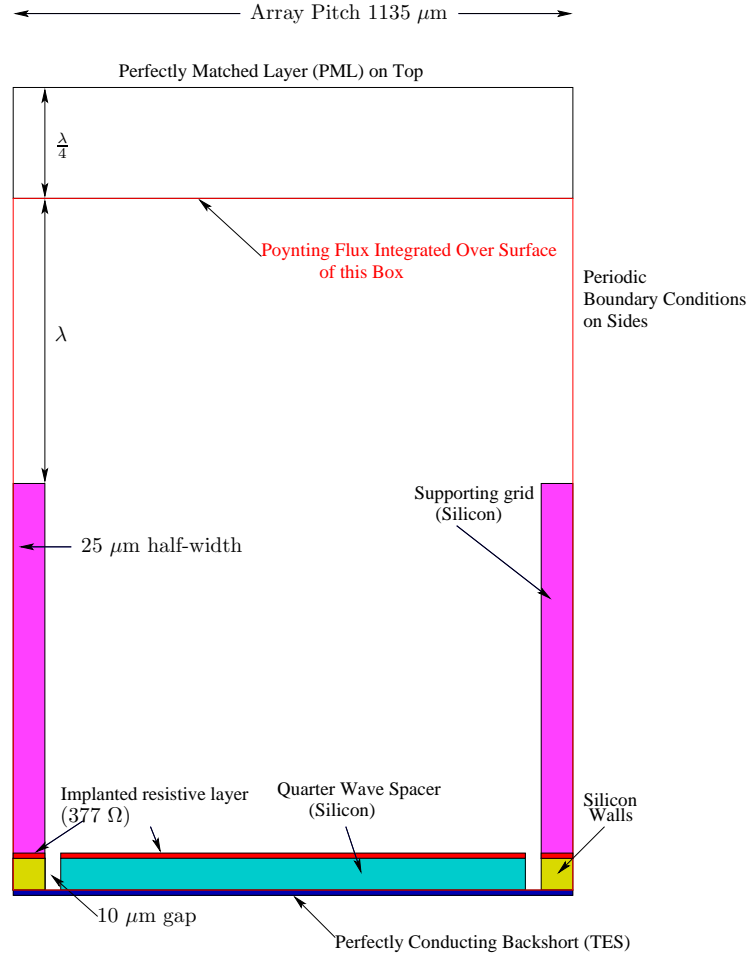


Figure 12. Pixel model corresponding to original pixel design. Note that the silicon support grid has been removed from the design and is omitted from simulations described here, unless otherwise stated.

The mechanical support grid also affects the angular dependence of the detector efficiency (see Figure 14). The grid structure behaves like a two-dimensional diffraction grating when the wavelength is smaller than the grid spacing. At both wavelengths (450 and $850\text{ }\mu\text{m}$) the array allows diffraction orders to propagate. This means that the non-absorbed reflected field is a superposition of the zeroth order (specular) component plus all the diffraction orders that can be generated. These depend on the frequency, angle of incidence and the grid spacing (i.e. the array pitch). HFSS models this behaviour in a region that is close to the array, i.e. in its near field. This means that we must be careful when comparing the simulations with experimental data. When we measure the reflected flux we can be in a far-field configuration where only the zeroth order is detected. In this case the HFSS results have to be processed to calculate the far-field in the periodic boundary case. The important point is that the method we have described to calculate the absorption remains correct.

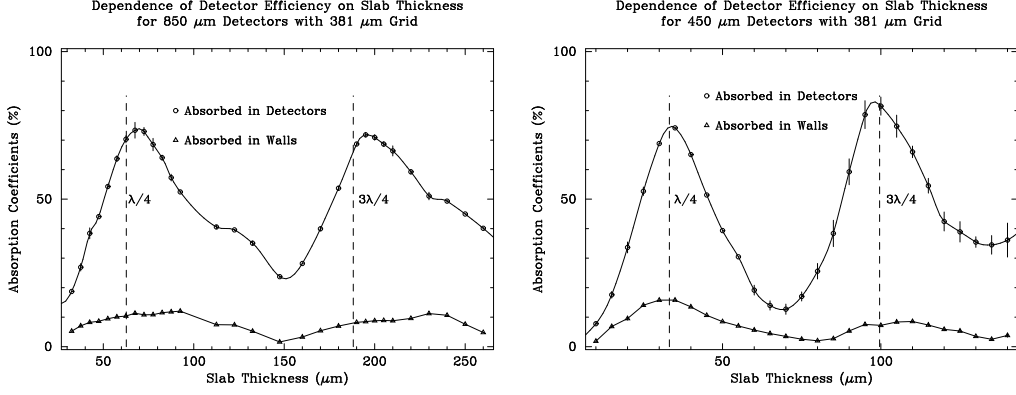


Figure 13. Predicted variation of detector efficiency with quarter-wave slab thickness for 850 μm (left) and 450 μm (right) detectors from HFSS simulations that include a 381 μm mechanical support grid. The vertical dashed lines correspond to the expected thicknesses for maximum efficiency.

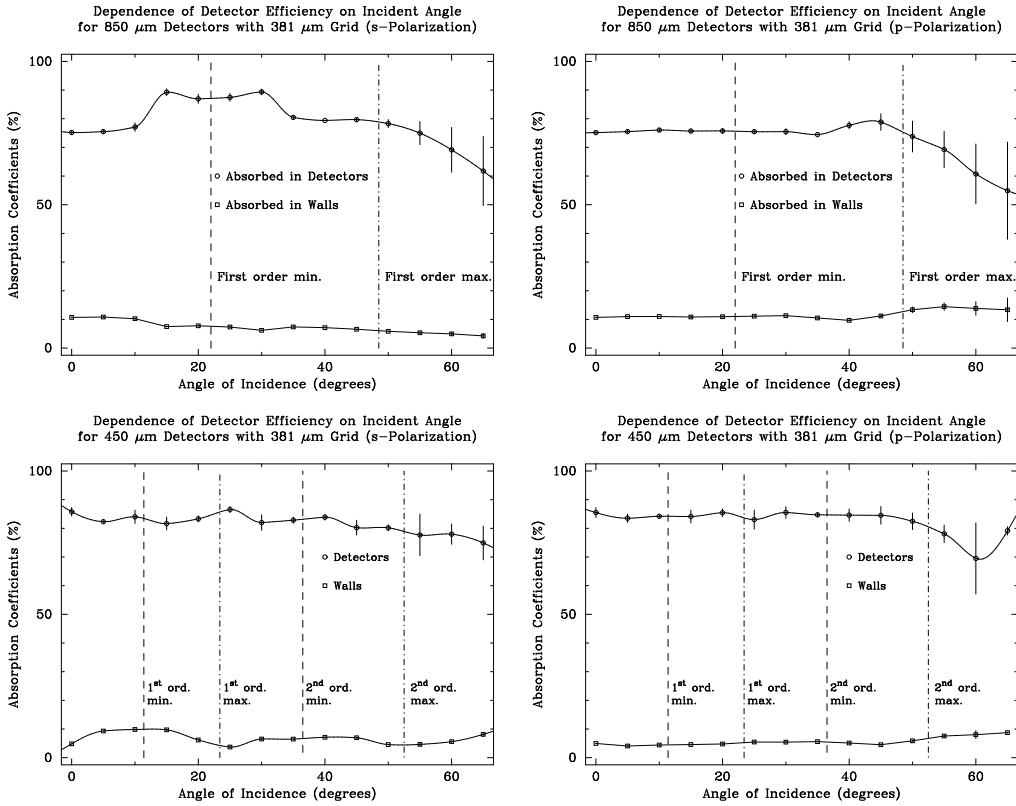


Figure 14. Predicted variation of 850 μm (top) and 450 μm detector efficiency with angle of incidence from HFSS simulations that include a 381 μm mechanical support grid. The vertical dashed lines represent the diffraction minima and maxima for the array pitch (1135 μm). Left: s-polarization. Right: p-polarization.

Because of its effect on the detector efficiency and because changes in the processing had made it redundant anyway we removed the mechanical support grid from the design.

4.4. Flatness of quarter-wave slab

We used the Ansoft Optimetrics package to investigate the effect of the top of the quarter-wave slab not being flat. To the top of the slab we added a wedge, and adjusted the thickness of the slab and that of the wedge,

keeping the mean thickness of the combined structure constant. This was done so that we could see the effects of having the top of the slab not parallel to the backshort, independent of changes in the thickness of the slab.

The top of the quarter-wave slab can make an angle of up to 1.6° with the backshort before reducing the absorption coefficient for the p-polarization by 5%. This corresponds to a deviation in the slab thickness of up to $\pm 15 \mu\text{m}$ across a pixel.

4.5. Effect of oxide layer

The fabrication process requires a layer of silicon oxide on the slab and walls as an etch stop. We ran simulations with a $1 \mu\text{m}$ thick layer of silicon dioxide on top of the walls and the slab. It had no significant effect on our results.

5. CONCLUSIONS

- The optimum quarter-wave slab thicknesses to attain at least 95% of the maximum efficiency are $66 \pm 6 \mu\text{m}$ and $99 \pm 3 \mu\text{m}$ for the 850 and 450 μm detectors, respectively.
- The optimum surface impedance is $377 \Omega/\square$. The absorption is not highly sensitive to the surface impedance. In order to attain at least 99% of the optimum efficiency the surface impedance must be between 309 and $460 \Omega/\square$ for the 850 μm detectors and between 308 and $461 \Omega/\square$ for the 450 μm detectors.
- The monochromatic efficiency of the detectors at the optimum slab thickness is 94%.
- When we take into account the finite bandwidth of the filters, the efficiency of the detectors at the optimum slab thickness is 93% at 850 μm and 88% at 450 μm .
- The detector efficiency is not very dependent on incident angle up to about 30° . There is no significant loss of sensitivity over the range of incident angles in the field of view.
- The flatness requirement for a decrease in efficiency of less than 5% is that the slab thickness varies across a pixel by no more than 15 μm .
- The presence of a $1 \mu\text{m}$ oxide layer on the walls and slab has a negligible effect on efficiency.
- The removal of the mechanical support grid improves the detector efficiency significantly.

We conclude from this modeling that the SCUBA-2 detectors will meet the requirement of an absorption efficiency of 75% or greater.

ACKNOWLEDGMENTS

SCUBA-2 is a collaboration between the UK Astronomy Technology Centre (Edinburgh), the National Institute for Standards and Technology (Boulder), the Scottish Microelectronics Centre (Edinburgh), the University of Wales (Cardiff), the Joint Astronomy Centre (Hawaii), the University of Waterloo, the University of British Columbia (Vancouver), the University of Lethbridge, Saint Mary's University (Halifax), and Université de Montréal. The project is funded by the UK Particle Physics and Astronomy Research Council, the JCMT Development Fund and the Canada Foundation for Innovation. HFSSTM and OptimetricsTM are trademarks of Ansoft Corporation. We would like to thank Kelvin Clarke at Ansoft for his help in troubleshooting the HFSS models.

REFERENCES

1. M. D. Audley, W. S. Holland, T. Hodson, M. J. MacIntosh, I. Robson, K. D. Irwin, G. C. Hilton, W. D. Duncan, A. Walton, W. Parkes, P. A. R. Ade, I. Walker, M. Fich, J. Kycia, M. Halpern, D. A. Naylor, G. Mitchell, and P. Bastien, “An update on the SCUBA-2 project.” SPIE 5498, in press, 2004.
2. L. N. Hadley and D. M. Dennison, “Reflection and Transmission Interference Filters Part I. Theory,” *J. Opt. Soc. Amer.* **37**(6), pp. 451–465, 1947.
3. B. Carli and D. Iorio-Fili, “Absorption of composite bolometers,” *J. Opt. Soc. Amer.* **71**(8), pp. 1020–1025, 1981.
4. W. Parkes, A. M. Gundlach, C. C. Dunare, J. G. Terry, J. T. M. Stevenson, A. J. Walton, and E. Schulte, “Realization of a large area microbolometer sensor array for submillimetre astronomy applications: SCUBA-2.” SPIE 5498, in press, 2004.